Accepted Manuscript

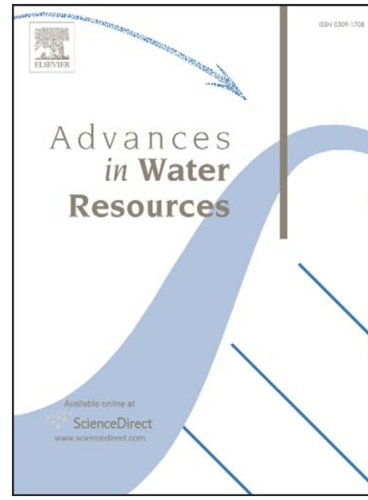

Effect of nonuniform boundary conditions on steady flow in saturated homogenous cylindrical soil columns

D.A. Barry

PII: S0309-1708(09)00003-7
DOI: 10.1016/j.advwatres.2009.01.003
Reference: ADWR 1382

To appear in: *Advances in Water Resources*

Received Date: 23 September 2008
Revised Date: 5 January 2009
Accepted Date: 7 January 2009

Effect of nonuniform boundary conditions on steady flow in saturated homogenous cylindrical soil columns

D.A. Barry*

Laboratoire de technologie écologique, Institut des sciences et technologies de l'environnement, Station 2, Ecole polytechnique fédérale de Lausanne, CH-1015 Lausanne, Switzerland

Submitted to: *Advances in Water Resources,* 23 September 2008

Revised and resubmitted: 5 January 2009

* Tel. +41 (21) 693-5576; fax. +41 (21) 693-5670; *E-mail address:* andrew.barry@epfl.ch

Abstract

Laboratory column experiments involving steady flow in homogeneous soil are often analyzed assuming that the flow is spatially uniform in any plane transverse to the longitudinal axis aligned with the column centerline. Axisymmetric steady flow in such a column was analyzed to determine the impact of radially nonuniform boundary conditions at the column entrance and exit planes. A general solution to the governing Laplace equation was derived taking into account arbitrary functional forms of the imposed head and flux boundary conditions. Specific solutions were deduced for smoothly varying and abrupt disturbances at the boundaries. The solutions were used to derive expressions for the length scale over which the induced flow nonuniformities are dissipated within the column. For soil columns with an aspect ratio (column radius/length) less than about $\frac{1}{3}$, the maximum dissipation length scale is in all cases less than $\frac{3}{2}R$, where R is the column radius. For practical purposes it is sufficient to take R as the dissipation length scale. Consequently, no matter what the radial variation in the boundary condition, flow will be uniform within the column if at each end a baffle zone with length equal to R is incorporated into the soil column design. The results can be applied to homogeneous anisotropic soil via a simple scaling. Published experimental results showing nonuniform flow near the entrance and exit boundaries were found to be consistent with the theoretical results.

Keywords: Bessel functions, Axisymmetric flow, Laplace's equation, Baffle, Orifice, Dissipation length scale, Analytical solutions, Stokes stream function, Hydraulic potential, Darcy's law, Streamlines, Fourier-Bessel series

1. Notation

C_1, C_2	Coefficients appearing in the separation-of-variables solution	
D_i	i^{th} coefficient in a Fourier-Bessel series	
E	Relative error	
E_i	i^{th} coefficient in a Fourier-Bessel series	L
f	Arbitrary function	
$\mathcal{F}_i$	i^{th} coefficient in a Fourier-Bessel series	
g	Head gradient, arbitrary function	
H	Heaviside step function,	
J_v	v^{th}-order Bessel function of the first kind	
K	Hydraulic conductivity	$\mathrm{LT^{-1}}$
K_{r^*}	Hydraulic conductivity in the r^* direction (anisotropic soil)	$\mathrm{LT^{-1}}$
K_{z^*}	Hydraulic conductivity in the z^* direction (anisotropic soil)	$\mathrm{LT^{-1}}$
L	Column length	L
L^*	Same as L except for an anisotropic soil	L
M	Dissipation factor	
q_r	Darcy flux in the r direction	$\mathrm{LT^{-1}}$
q_z	Darcy flux in the z direction	$\mathrm{LT^{-1}}$
$q_{z=0}^{av}$	Average Darcy longitudinal flux at $z = 0$	$\mathrm{LT^{-1}}$
r	Radial distance from column centerline	L
r_n	Radius of the orifice at the $z = 0$ column boundary	L
r^*	Same as r except for an anisotropic soil	L
R	Column radius	L
R^*	Same as R except for an anisotropic soil	L
$\mathcal{R}$	Intermediate function used in the separation-of-variables solution	

z	Distance from end of soil column	L
z^*	Same as z except for an anisotropic soil	L
Z	Intermediate function used in the separation-of-variables solution	
Greek		
α_i	i^{th} non-negative root of J_1	
ϕ	Hydraulic head	L
ϕ_L	Boundary condition, hydraulic head applied at $z = L$	L
ϕ_L^{av}	Average head at $z = L$	L
ψ	Stokes stream function	L^3T^{-1}

2. Introduction

Laboratory soil columns are used frequently to determine experimentally vadose zone and aquifer hydraulic and chemical transport properties (e.g., [8][15][21][25][38]). Soils used in such experiments can be undisturbed field samples or, alternatively, samples that are pre-treated and, perhaps, homogenized prior to use. Data collected from laboratory experiments are usually analyzed assuming one-dimensional flow conditions exist in the soil column (e.g., [4][24][33][34][37]), i.e., variations in hydraulic and other properties, as well as the flow within the column, are taken as negligible. Despite a large body of research and applications of soil column experiments dating back at least 50 y (e.g., [7][10][17]), research on their use continues. For instance, Massabò et al. [26] reported a laboratory column method for determination of transverse solute dispersivity. Their method relies explicitly on uniform background flow. Recently, Wang and Persaud [36] investigated solute injection into an already established spatially uniform flow field in a soil column.

Uniform steady flow throughout a laboratory column, although conceptually simple and of great practical value, is difficult to attain in practice. This is particularly so for experiments where a high water flux is specified at a boundary since intuitively it would be expected that any spatial variability in the applied flux would persist a substantial distance into the soil. Specification of the steady water flux through a soil column is beneficial to investigate, for example, velocity-dependent dispersion in porous media (e.g., [2][13][28][29]) or water phase/soil reactive chemistry (e.g., [3][27][35]). For specified-flux experiments, water is injected into the column at a fixed rate, typically using a supply tube with a diameter less than the column apparatus (Fig. 1). Unless the injected flow is baffled before entering the soil, the flux into the soil will be nonuniform [22]. Even experiments that are designed with fixed hydraulic head conditions at the column entrance and exit can be affected by nonuniformity in the flow field due to local variability in the materials comprising the boundaries of the column apparatus through which the water flows [32], or because water in the supply reservoir adjoining the column is not hydrostatic.

Given that soil column experiments utilizing homogeneous media are common, it is beneficial to understand quantitatively factors that affect the results obtained from them. Here, the flow patterns at the soil column entrance and exit are investigated. The specific goal of this study is to model explicitly nonuniform boundary conditions in steady-flow soil column experiments and, based on the model, examine features of induced nonuniform flow fields within the soil column, in particular the spatial extent over which disturbances introduced at the boundaries dissipate.

3. Theoretical model

Axisymmetric flow in a cylinder containing a homogeneous soil, as depicted in Fig. 1, is considered. The assumption of symmetry about the z-axis means that, for planes at fixed z, radial, but not angular, variations are permitted.

Steady flow in homogeneous soil is governed by Laplace's equation (e.g., [6]), which in axisymmetric cylindrical coordinates is given by (e.g., [31]):

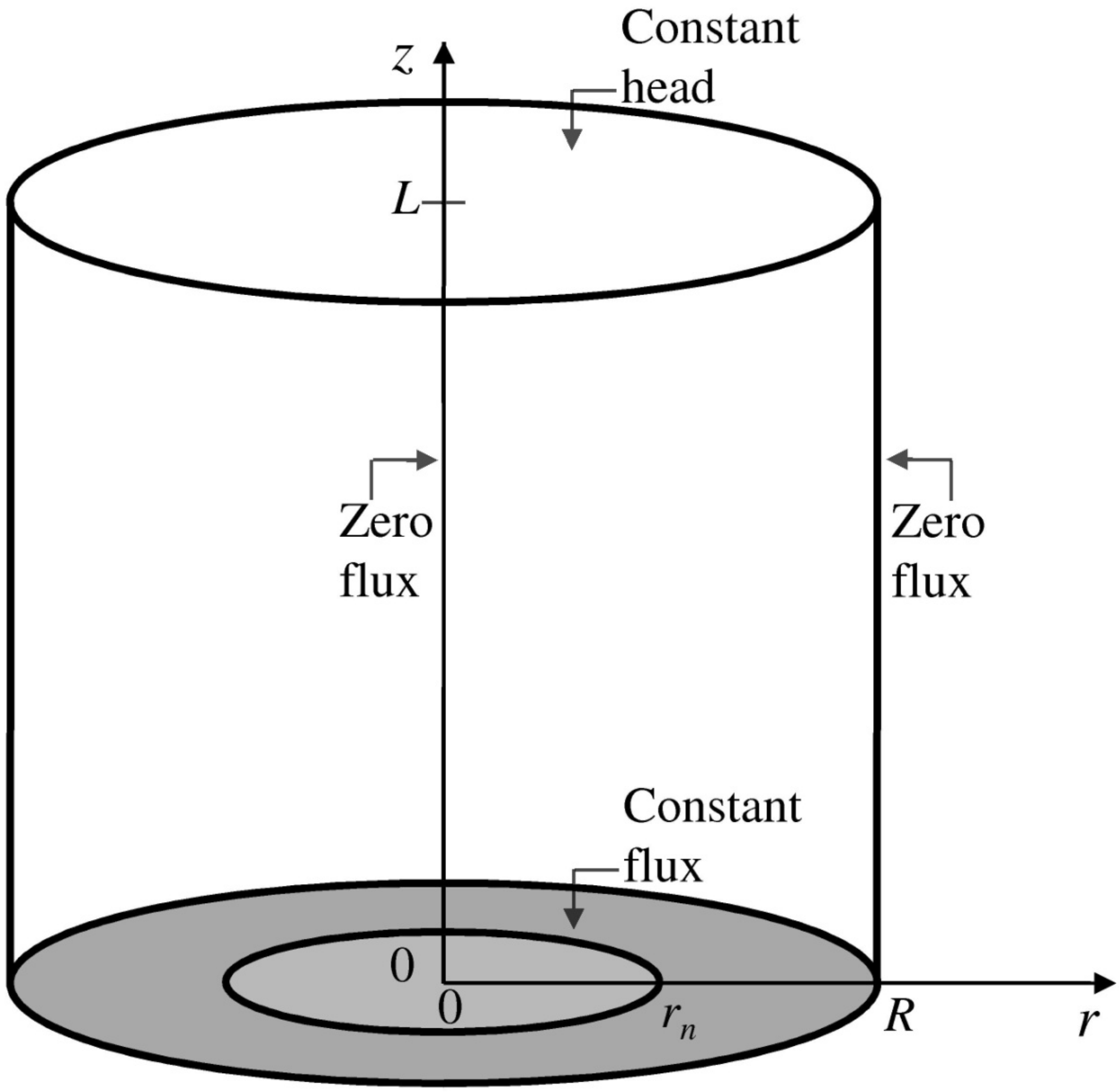

Fig. 1. Diagram of the soil column, coordinate axes and boundary conditions used in the analytical model. The head and flux conditions are constant in time, but vary arbitrarily with r. In addition to the general head and flux conditions, at $z = 0$ a particular flux condition is indicated, i.e., an inlet/exit port of radius r_n, within which the longitudinal flux is spatially uniform and steady. For this case, in the region $r_n \leq r < R$, the longitudinal flux is zero.

$$\frac{1}{r}\frac{\partial}{\partial r}\left(r\frac{\partial \phi}{\partial r}\right) + \frac{\partial^2 \phi}{\partial z^2} = 0, 0 < r < R, 0 < z < L, \tag{1}$$

where $\phi \equiv \phi(r, z)$ [L] is the hydraulic head, r [L] is the radial distance and z [L] is the longitudinal distance. The soil column has length L [L] and radius R [L], and the coordinate system origin is located at $(r, z) = (0,0)$, as shown in Fig. 1. Eq. (1) is solved subject to:

$$\frac{\partial\phi}{\partial r} = 0, r = 0, 0 < z < L, \tag{2}$$

$$\frac{\partial\phi}{\partial r} = 0, r = R, 0 < z < L, \tag{3}$$

$$\frac{\partial\phi}{\partial z} = g(r), 0 < r < R, z = 0 \tag{4}$$

and

$$\phi = \phi_L(r), 0 < r < R, z = L. \tag{5}$$

Eq. (2), arising from the axial symmetry, states that there is zero flux across the centerline of the column, while Eq. (3) accounts for the column's solid wall where the radial flux is zero (Fig. 1). At $z = 0$ the gradient is specified. Since this is proportional to the flux in the z-direction, using Eq. (4) the longitudinal flux at $z = 0$ is specified as an arbitrary function of r. The sign of the flux can be positive or negative, thus in Fig. 1 either column end can be the column entrance or exit, or flow can enter and exit both ends simultaneously, depending on the functions in Eqs. (4) and (5). Since, for steady flow, the total flux across any plane defined by a fixed value of z is constant, it is redundant to specify the flux at both ends of the column. Thus, at $z = L$ the hydraulic head is given as an arbitrary function of r in Eq. (5).

Eqs. (1) – (5) are written for an isotropic medium. However, the same model can be considered as being a scaled version of an anisotropic homogeneous medium with hydraulic conductivity K_{z^*} in the z^* direction and K_{r^*} in the r^*direction, where the principle directions are assumed to be aligned with the column's longitudinal and transverse axes. If the anisotropic homogeneous medium variables are identified with an asterisk, then the mapping between the scaled and asterisked models is given by $z = z^*, L = L^*, \sqrt{K_{r^*}}r = \sqrt{K_{z^*}}r^*$ and $K_{r^*}R = \sqrt{K_{z^*}}R^*$.

The solution satisfying Eqs. (1) – (5) is detailed in Appendix 1 as:

$$\frac{\phi}{R} = \frac{2}{R^2}\int_0^R \left[\frac{\phi_L(r)}{R} - \frac{(L-z)}{R} g(r)\right] r\mathrm{d}r - \sum_{i=2}^{\infty} \frac{\frac{D_i}{\alpha_i}\sinh\left(\alpha_i \frac{L-z}{R}\right) - \frac{E_i}{R}\cosh\left(\alpha_i \frac{z}{R}\right)}{\cosh\left(\alpha_i \frac{L}{R}\right)} \mathrm{J}_0\left(\alpha_i \frac{r}{R}\right), \tag{6}$$

where J_0 is the zero-order Bessel function of the first kind and α_i is the i^{th} nonnegative root of the first-order Bessel function of the first kind, J_1. As mentioned in Appendix 1, D_i and E_i in Eq. (6) can be calculated from Eq. (40) upon specification of the functional forms of $g(r)$ and $\phi_L(r)$, respectively, in Eqs. (4) and (5), i.e.,

$$D_i = \frac{2}{\mathrm{J}_0^2(\alpha_i)R^2}\int_0^R g(r)\mathrm{J}_0\left(\alpha_i \frac{r}{R}\right) r\mathrm{d}r\,, i = 2, 3, \cdots \tag{7}$$

and

$$\frac{E_i}{R} = \frac{2}{\mathrm{J}_0^2(\alpha_i)R^2}\int_0^R \frac{\phi_L(r)}{R}\mathrm{J}_0\left(\alpha_i \frac{r}{R}\right) r\mathrm{d}r, i = 2, 3, \cdots. \tag{8}$$

All variables with dimensions of length become dimensionless by scaling with R, e.g., geometric variables controlling the solution can be taken as $\frac{z}{R}$, $\frac{L}{R}$ and $\frac{r}{R}$. An alternative would be to use L as the normalizing length, although R is preferred here. The dimension of time enters the problem specification via the hydraulic conductivity, K, and the applied flux (resulting from specifying the gradient) at the $z = 0$ boundary. Therefore, the natural scaling variable to remove the time dimension is K. The results are presented in dimensional form to facilitate their physical interpretation. However, for analysis of the results presented below, the scaling with R of geometrical variables and hydraulic head is useful, as is the scaling of flux by K.

3.1. Stokes stream function

The Darcy flux components in the z and r directions are calculated from ϕ in Eq. (6) as, respectively (e.g., [6]):

$$q_z(r,z) = -K\frac{\partial \phi}{\partial z} = \frac{1}{r}\frac{\partial \psi}{\partial r} \tag{9}$$

and

$$q_r(r,z) = -K\frac{\partial \phi}{\partial r} = -\frac{1}{r}\frac{\partial \psi}{\partial z}. \tag{10}$$

The second equalities in Eqs. (9) and (10) define the Stokes stream function, $\psi \equiv \psi(r,z)$ (e.g., [5][19]). Contours of constant ψ are perpendicular to contours of constant ϕ. From Eqs. (6), (9) and (10), ψ (or $\frac{\psi}{KR^2}$ in dimensionless form) is:

$$-\frac{\psi}{KR^2} = \frac{r^2}{R^4}\int_0^R g(r)r\mathrm{d}r + \frac{r}{R}\sum_{i=2}^{\infty}\frac{\frac{D_i}{\alpha_i}\cosh\left(\alpha_i\frac{L-z}{R}\right)+\frac{E_i}{R}\sinh\left(\alpha_i\frac{z}{R}\right)}{\cosh\left(\alpha_i\frac{L}{R}\right)}\mathrm{J}_1\left(\alpha_i\frac{r}{R}\right). \tag{11}$$

4. Applications

The above results are used to provide exact solutions for hydraulic head and Stokes stream function for two applications involving nonuniform boundary conditions. The first involves smooth variations at $z = 0$ and L and the second an abrupt variation. In both cases the longitudinal length scale of the variations induced on the flow in the soil column is evaluated analytically.

4.1. Smooth variation in boundary conditions

In this section a simple special case is used to provide some insight into the above analytical results. Because Bessel functions are orthogonal (e.g., [39]), choosing boundary conditions in the form of a suitable Bessel function means that the summations appearing in the coefficient equations (7) and (8) are zero except for a single term. For this purpose, the head at $z = L$ is taken in Eq. (5) as:

$$\frac{\phi(r,L)-\phi(R,L)}{\phi(0,L)-\phi(R,L)} = \frac{\mathrm{J}_0\left(\alpha_i\frac{r}{R}\right)-\mathrm{J}_0(\alpha_i)}{1-\mathrm{J}_0(\alpha_i)}, 0 < r < R, \tag{12}$$

where $\phi(0,L)$ and $\phi(R,L)$ denote the imposed values of $\phi(r,L)$ at $r = 0$ and R, respectively. The most useful case is perhaps for $i = 2$, for which case the right side of Eq. (12) varies monotonically with r and lies in the range (0,1). Consequently, the applied head at $z = L$ lies in the range bounded by $\phi(0, L)$ and $\phi(R, L)$. By adjusting $\phi(0, L)$ and $\phi(R, L)$, Eq. (12) gives a monotonically increasing or decreasing head profile with increasing r. For $i = 3, 4, \cdots$, the function on the right side of Eq. (12) is nonmonotonic. To analyze the effect of the boundary conditions, it is sufficient to take the monotonic case in Eq. (12). Note that, in applying the boundary condition (12), the absolute values of $\phi(0, L)$ and $\phi(R, L)$ are irrelevant since the flow is governed by head differences and, in any case, the head is measured relative to an arbitrary reference pressure and elevation.

The average head, ϕ_L^{av}, applied to the surface at $z = L$ is given by:

$$\frac{\phi_L^{av}}{R} = \frac{1}{\pi R^2}\int_0^{2\pi}\int_0^R \frac{\phi(r, L)}{R} r\mathrm{d}r\mathrm{d}\theta = \frac{2}{R^2}\int_0^R \frac{\phi(r, L)}{R} r\mathrm{d}r. \quad (13)$$

Using Eq. (12) in Eq. (13) gives:

$$\frac{\phi_L^{av} - \phi(R, L)}{\phi(0, L) - \phi(R, L)} = -\frac{\mathrm{J}_0(\alpha_i)}{1 - \mathrm{J}_0(\alpha_i)}, \quad (14)$$

where $\phi(0, L)$ and $\phi(R, L)$ are the imposed heads at $z = 0$ and L, respectively. For $i = 2$, the right side of Eq. (14) is approximately 0.3. Due to the circular geometry and the monotonic change for this case, the average head is dominated by the head applied at $r = R$ rather than that at $r = 0$.

The same functional form as for the head boundary condition is chosen for the flux condition applied at $z = 0$. From Eqs. (4), (9) and (12) this flux is:

$$\frac{-Kg(r) - q_z(R, 0)}{q_z(0,0) - q_z(R, 0)} = \frac{\mathrm{J}_0\left(\alpha_j \frac{r}{R}\right) - \mathrm{J}_0(\alpha_j)}{1 - \mathrm{J}_0(\alpha_j)}, 0 < r < R. \quad (15)$$

In Eq. (15), the applied longitudinal flux $q_z(r, 0) = -Kg(r)$ lies in the range bounded by $q_z(0,0)$ and $q_z(R, 0)$, where $q_z(0,0)$ is the imposed longitudinal flux at $r = 0$ and $q_z(R, 0)$ is that at $r = R$. In the solution presented below, α_i and α_j are allowed to take different values in Eqs. (12) and (15) although in the analysis this is not particularly useful. The flow direction depends on the signs of $q_z(0,0)$ and $q_z(R,0)$. If both are positive then the flow is in the direction of increasing z and vice versa. The interpretation of average flux calculated from Eq. (15) is the same as that for the average head discussed above. In particular, corresponding to Eq. (14), the average flux, $q_{z=0}^{av}$, is:

$$\frac{q_{z=0}^{av} - q_z(R,0)}{q_z(0,0) - q_z(R,0)} = -\frac{\mathrm{J}_0(\alpha_i)}{1 - \mathrm{J}_0(\alpha_i)}. \tag{16}$$

With the boundary conditions as specified in Eqs. (12) and (15), Eq. (6) becomes:

$$\begin{aligned} \frac{\phi - \phi(R,L)}{\phi(0,L) - \phi(R,L)} &= \frac{(L-z)}{[\phi(0,L) - \phi(R,L)]}\frac{q_z(R,0)}{K} \\ &+ \frac{1}{1 - \mathrm{J}_0(\alpha_i)}\left[\frac{\cosh\left(\alpha_i \frac{z}{R}\right)}{\cosh\left(\alpha_i \frac{L}{R}\right)}\mathrm{J}_0\left(\alpha_i \frac{r}{R}\right) - \mathrm{J}_0(\alpha_i)\right] \\ &+ \frac{[q_z(0,0) - q_z(R,0)]R}{K[\phi(0,L) - \phi(R,L)][1 - \mathrm{J}_0(\alpha_j)]}\left[\frac{\sinh\left(\alpha_j \frac{L-z}{R}\right)}{\cosh\left(\alpha_j \frac{L}{R}\right)}\frac{\mathrm{J}_0\left(\alpha_j \frac{r}{R}\right)}{\alpha_j} \right. \\ &\left. - \frac{(L-z)}{R}\mathrm{J}_0(\alpha_j)\right]. \end{aligned} \tag{17}$$

From Eq. (11), the stream function corresponding to Eq. (17) is:

$$\begin{aligned} \frac{\psi}{KR^2} = \frac{r^2}{2R^2}&\left\{\frac{q_z(R,0)}{K} - \frac{[q_z(0,0) - q_z(R,0)]\mathrm{J}_0(\alpha_j)}{K[1 - \mathrm{J}_0(\alpha_j)]}\right\} \\ &+ \frac{r}{R}\left\{\frac{[q_z(0,0) - q_z(R,0)]}{K[1 - \mathrm{J}_0(\alpha_j)]\alpha_j}\frac{\cosh\left(\alpha_j \frac{L-z}{R}\right)}{\cosh\left(\alpha_j \frac{L}{R}\right)}\mathrm{J}_1\left(\alpha_j \frac{r}{R}\right)\right. \\ &\left. - \frac{[\phi(0,L) - \phi(R,L)]}{R[1 - \mathrm{J}_0(\alpha_i)]}\frac{\sinh\left(\alpha_i \frac{z}{R}\right)}{\cosh\left(\alpha_i \frac{L}{R}\right)}\mathrm{J}_1\left(\alpha_i \frac{r}{R}\right)\right\}. \end{aligned} \tag{18}$$

Eq. (17) is now used to evaluate the effect of the nonuniform boundary conditions at $z = 0$ and L. The solution is analyzed for the case where the soil column is assumed to have a small aspect ratio, i.e., $\frac{R}{L} \ll 1$, so that the nonuniformities introduced by the boundary conditions do not interact. This assumption means that each boundary condition can be examined independently, with the other boundary condition considered as being uniform. An estimate of the value of $\frac{R}{L}$ for which the boundary conditions do not interact is deduced also.

Consider first the head condition, Eq. (14). As noted above, for $i = 2$ the right side of this condition has a range of unity. The disturbance is at its maximum at $z = L$, where the boundary condition is applied. Inside the column, the head differences induce flow leading to dissipation of the disturbance, the magnitude of the latter decreasing with decreasing z (i.e., increasing distance away from the boundary). For fixed $z \leq L$, the range of the head variation normalized by the initial disturbance is $\frac{\phi(0,z)-\phi(R,z)}{\phi(0,L)-\phi(R,L)}$. Taking $q_z(0,0) = q_z(R,0)$ to remove the impact of variations in the boundary condition at $z = 0$, and using the aspect ratio condition, Eq. (17) yields for $i = 2$:

$$\frac{\phi(0,z) - \phi(R,z)}{\phi(0,L) - \phi(R,L)} \approx \exp\left(-\alpha_2 \frac{L - z}{R}\right). \tag{19}$$

An exact expression for this quantity is derived in Appendix 3. If the initial disturbance is considered as dissipated when it is reduced by, say, a factor of M, then from Eq. (19) this occurs at:

$$z = L - \frac{R}{\alpha_2} \ln(M). \tag{20}$$

Taking, e.g., $M = 50$ gives the remarkably simple result:

$$z \approx L - R, \tag{21}$$

i.e., the disturbance propagates a longitudinal distance R from the boundary at $z = L$ into the column. For $M = 100$, Eq. (21) becomes $z \approx L - 1.2R$.

The disturbance due to a nonuniform flux condition at $z = 0$ and a uniform head condition at $z = L$ is treated similarly. The result is (Appendix 3):

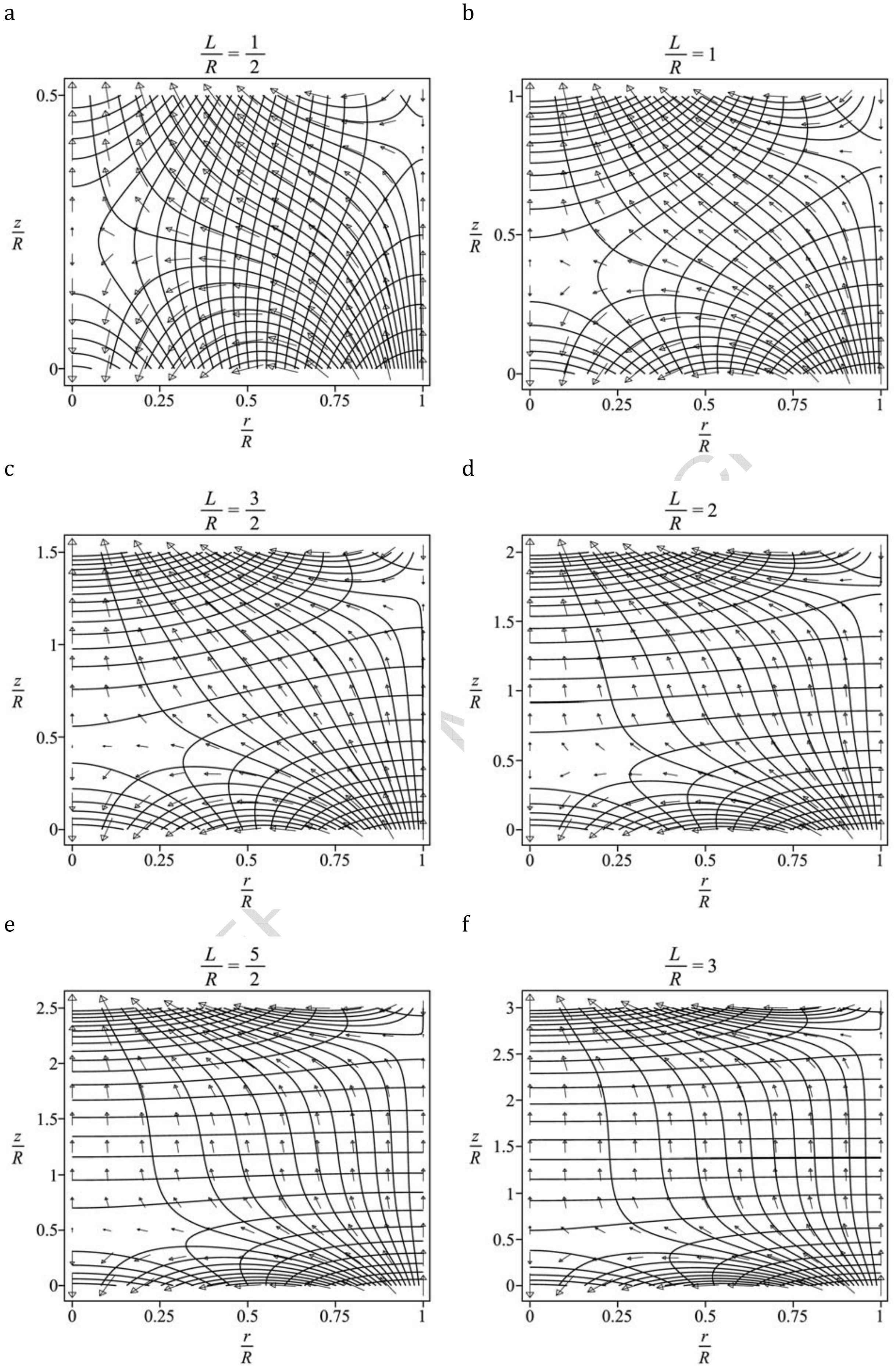
a
$\frac{L}{R} = \frac{1}{2}$
b
$\frac{L}{R} = 1$
c
$\frac{L}{R} = \frac{3}{2}$
d
$\frac{L}{R} = 2$
e
$\frac{L}{R} = \frac{5}{2}$
f
$\frac{L}{R} = 3$
$\frac{z}{R}$
$\frac{r}{R}$
0
0.25
0.5
0.75
1

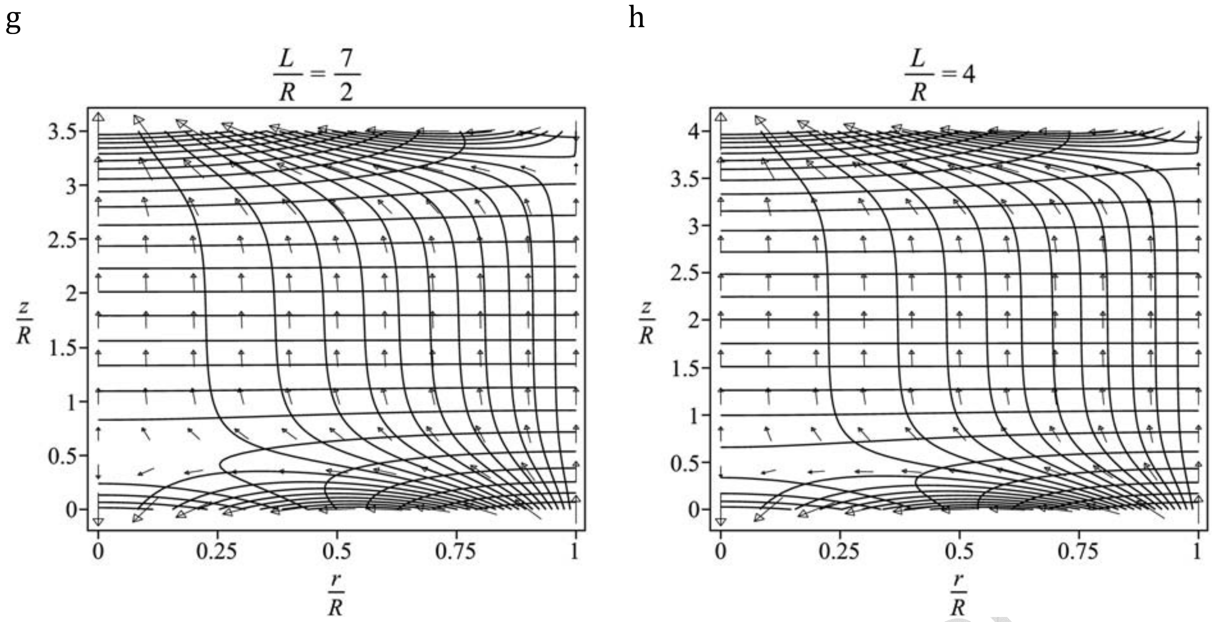

Fig. 2. Darcy flux vectors (arrows), hydraulic head contours and streamlines (lines parallel to flux vectors) calculated for the solution presented in §4.1, Eqs. (17) and (18). Parameters used: $i = j = 2$, $\frac{q_z(0,0)}{K} = -3$, $\frac{q_z(0,R)}{K} = 2$, $\frac{\phi(0,L)}{R} = -2.3$ and $\frac{\phi(R,L)}{R} = -1$. The sequence of plots a-h shows the effect of decreasing the aspect ratio, $\frac{R}{L}$. From $\frac{L}{R} = 2$ to $\frac{L}{R} = 2.5$ (plots d and e) the disturbances from each boundary no longer interact whereas the interaction is clear for plots a – c. For $\frac{L}{R} \geq 3$ (plots f – h), the disturbed zones at each end of the flow domain do not, for practical purposes, interact, and in each case a zone of uniform flow is evident within the column.

$$\frac{\phi(0,z) - \phi(R,z)}{\phi(0,0) - \phi(R,0)} \approx \exp\left(-\alpha_2 \frac{z}{R}\right). \tag{22}$$

Perhaps not surprisingly given Eq. (19), Eq. (22) gives the characteristic distance that the nonuniform flow persists in the column from the boundary at $z = 0$ is:

$$z \approx R, \tag{23}$$

where, as above, a factor of 50 reduction has been used.

Below Eqs. (1) – (5) the scaling to an anisotropic homogeneous medium (denoted by an asterisk) was given. For that case, Eq. (23) becomes:

$$z^* \approx \sqrt{\frac{K_{z^*}}{K_{r^*}}} R^*. \tag{24}$$

As the transverse hydraulic conductivity, K_{r^*}, increases relative to the longitudinal hydraulic conductivity, K_z^*, the dissipation length scale decreases. Physically, this is in agreement with intuition, i.e., as the longitudinal flux decreases relative to the radial flux, the disturbance attenuation length scale decreases also. The same interpretation applies to the anisotropic version of Eq. (21).

An example of the head contours, Darcy flux vectors and Stokes stream function calculated from the results in this section is presented in Fig. 2. The plots show the effect of decreasing the aspect ratio $\frac{R}{L}$ (plot headings show the value of the inverse of the aspect ratio, $\frac{L}{R}$), with other parameter values given in the caption held constant. The imposed flux at $z = 0$ changes sign in order to display an extreme case of variability in the flux boundary condition, wherein each boundary acts as both an inflow and outflow boundary. Clearly, both boundary conditions (12) and (15) induce a degree of complexity in the flow patterns in the regions adjacent to each boundary. However, as given by Eqs. (21) and (23), at a distance $z \approx R$ away from each boundary a uniform flow pattern is established for small enough aspect ratios.

In order to evaluate in more detail the dissipation length scale estimates given above, the reduction in maximum radial flux, q_r, with z was examined for the case in Fig. 2. The results were normalized by the corresponding value at $z = 0$, with results plotted in Fig. 3. This metric was chosen because the maximum radial flux will monotonically decrease as the flow becomes more uniform with z, independent of the form of the disturbance at $z = 0$. As mentioned in the Fig. 3 caption, this example was constructed such that the head difference at the $z = L$ boundary induces the same maximum q_r there as at $z = 0$. This simply facilitates the interpretation of the plot. The plots in Fig. 3 confirm what is shown in Fig. 2, i.e., up to $\frac{L}{R} \approx 2.5$, the boundary disturbances interact, but as the boundaries separate further, the presence of a zone of uniform flow emerges. For example, in Fig. 3, the curve for $\frac{L}{R} = 3$ shows that there is a zone of uniform flow (as defined by the factor 50 reduction) in the region $1 < \frac{z}{R} < 2$.

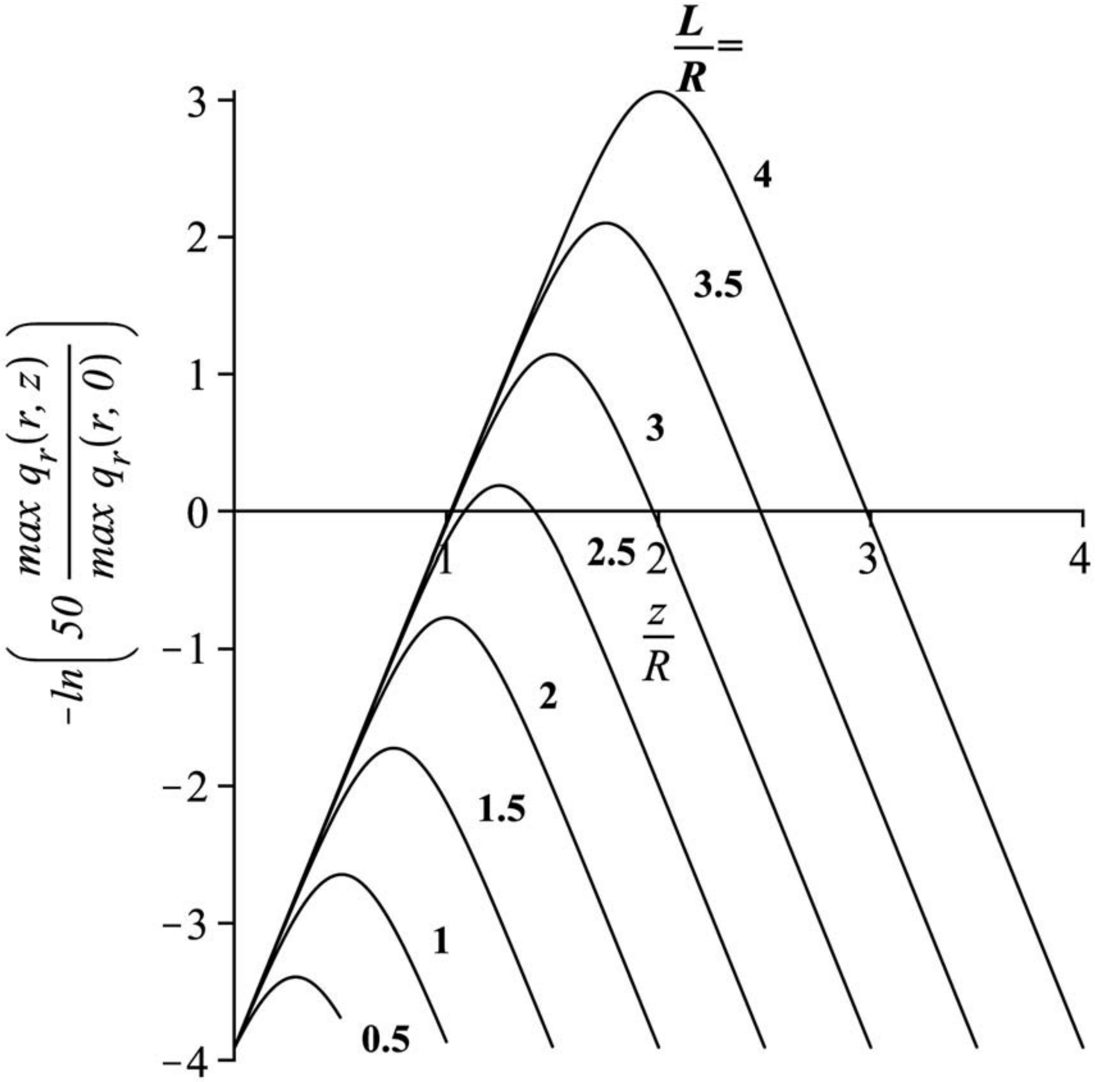

Fig. 3. Reduction of the maximum radial flux, q_r, normalized by the maximum radial flux at the $z = 0$ boundary, for the plots presented in Fig. 2, as identified by the curve labels showing the values of $\frac{L}{R}$. Note that the case in Fig. 2 was constructed so that the maximum radial flux at $\frac{z}{R} = 0$ is very close to that at $\frac{L}{R}$. The factor 50 used in the vertical axis translates the results along the vertical axis such that the horizontal axis marks the transition between a reduction factor of less than 50 (zone below the horizontal axis) and greater than 50 (zone above the horizontal axis). The straight segments of each curve have slopes that are close to $\pm\alpha_2 \approx \pm 3.8$, confirming the exponential dissipation behavior given by Eqs. (19) and (22).

4.2. Abrupt variation in the flux condition

In §4.1 the boundary conditions modeled smooth variations in the applied head and flux. In this section the extreme case of a discontinuous longitudinal flux at $z = 0$ is considered, the origin of which is depicted in Fig. 1. This situation arises, of course, when water is added or removed from the column through an orifice with a radius less than the column radius. The discontinuity in flux occurs at the orifice boundary ($r = r_n$). Sometimes, experimental columns include a baffle region between the column end and the soil. Here, it is assumed that no baffle region exists so that the nonuniform flow induced by the boundary condition can reach its maximum extent within the column. That is, depending on the flow direction, at $z = 0$ the flow enters or exits the column directly in the zone $0 < r < r_n$ (Fig. 1), with the rest of the boundary $r_n \leq r < R$ impervious to flow. Variability in the head condition at $z = L$ is not considered since, as seen in §4.1, for small aspect ratios, the boundary conditions can be examined separately. Thus, the case of the orifice shown in Fig. 1 can be modeled by solving Eq. (1) subject to Eqs. (2), (3) and:

$$-K\frac{\partial \phi}{\partial z} = Q\frac{R^2}{r_n^2}[1 - \mathrm{H}(r - r_n)], z = 0, 0 < r < R, \tag{25}$$

where Q is constant and H is the Heaviside step function, along with:

$$\phi = \phi_L, z = L, 0 < r < R, \tag{26}$$

where ϕ_L is a constant. In Eq. (25), the factor containing the Heaviside step function ensures the longitudinal flux in the region $r_n \leq r < R$ is zero, as desired. In this same equation, the total flux entering the column is $\pi R^2 Q$. The supply/drainage orifice has an area of πr_n^2, so the flux per unit area entering the column is $Q\frac{R^2}{r_n^2}$, as given in Eq. (25). The solution is again derived from Eq. (6):

$$\frac{(\phi - \phi_L)}{L}\frac{K}{Q} = 1 - \frac{z}{L} + \frac{2R^2}{Lr_n}\sum_{i=2}^{\infty}\frac{\mathrm{J}_1\left(\alpha_i \frac{r_n}{R}\right)}{\alpha_i^2 \mathrm{J}_0^2(\alpha_i)}\frac{\sinh\left(\alpha_i \frac{L-z}{R}\right)}{\cosh\left(\alpha_i \frac{L}{R}\right)}\mathrm{J}_0\left(\alpha_i \frac{r}{R}\right), \tag{27}$$

with the corresponding Stokes stream function:

$$\frac{\psi}{QR^2} = \frac{r^2}{2R^2} + \frac{2r}{r_n}\sum_{i=2}^{\infty}\frac{\mathrm{J}_1\left(\alpha_i \frac{r_n}{R}\right)}{\alpha_i^2 \mathrm{J}_0^2(\alpha_i)}\frac{\cosh\left(\alpha_i \frac{L-z}{R}\right)}{\cosh\left(\alpha_i \frac{L}{R}\right)}\mathrm{J}_1\left(\alpha_i \frac{r}{R}\right). \tag{28}$$

The semi-infinite solutions corresponding to Eqs. (27) and (28), found for the limit $L \to \infty$, are, respectively:

$$\frac{\phi}{R}\frac{K}{Q}+\frac{z}{R}=\frac{2R}{r_n}\sum_{i=2}^{\infty}\frac{\mathrm{J}_1\left(\alpha_i\frac{r_n}{R}\right)}{\alpha_i^2\mathrm{J}_0^2(\alpha_i)}\exp\left(-\alpha_i\frac{z}{R}\right)\mathrm{J}_0\left(\alpha_i\frac{r}{R}\right) \tag{29}$$

and

$$\frac{\psi}{QR^2}=\frac{r^2}{2R^2}+\frac{2r}{r_n}\sum_{i=2}^{\infty}\frac{\mathrm{J}_1\left(\alpha_i\frac{r_n}{R}\right)}{\alpha_i^2\mathrm{J}_0^2(\alpha_i)}\exp\left(-\alpha_i\frac{z}{R}\right)\mathrm{J}_1\left(\alpha_i\frac{r}{R}\right). \tag{30}$$

Eqs. (29) and (30) show that the disturbance introduced at the boundary $z=0$ dissipates away from the boundary according to $\exp\left(-\alpha_i\frac{z}{R}\right)$. Since the α_i are strictly positive and increase with i, to a first approximation this dissipation is controlled by the first term in the summations in Eqs. (29) and (30), i.e., $\exp\left(-\alpha_2\frac{z}{R}\right)$, consistent with what was found in §4.1

Returning to the finite length column, it is assumed as before that it has a small aspect ratio, in which case the summation in Eq. (27) is rapidly convergent except in the vicinity of the boundary at $z=0$. This is not surprising since the boundary condition there is a step function. Although this creates a computational issue in calculating solutions in the vicinity of the $z=0$ boundary, it does not affect the estimation of the persistence of the nonuniform flux condition within the soil column some distance from it. At $z=0$, the discontinuous boundary condition (25) introduces a monotonic head variation of magnitude $|\phi(0,0)-\phi(R,0)|$. As shown in the following, the characteristic longitudinal decay length turns out to be identical to that calculated previously, i.e., Eqs. (22) and (23). This is consistent with Eq. (29), which indicates that the first term in the summation dominates its convergence, a property that is checked in some detail below.

The result that the dissipation is approximated by $\exp\left(-\alpha_2\frac{z}{R}\right)$ is, perhaps, counter-intuitive since the boundary condition (25) shows that the flux into the column becomes unbounded as the orifice size decreases, i.e., $r_n\to 0$. However, the dissipation of this disturbance as it propagates into the column is controlled by the radial flux, which is proportional to $\frac{\partial\phi}{\partial r}$. Because the radial gradient is very large for a large flux, so too is the dissipation rate.

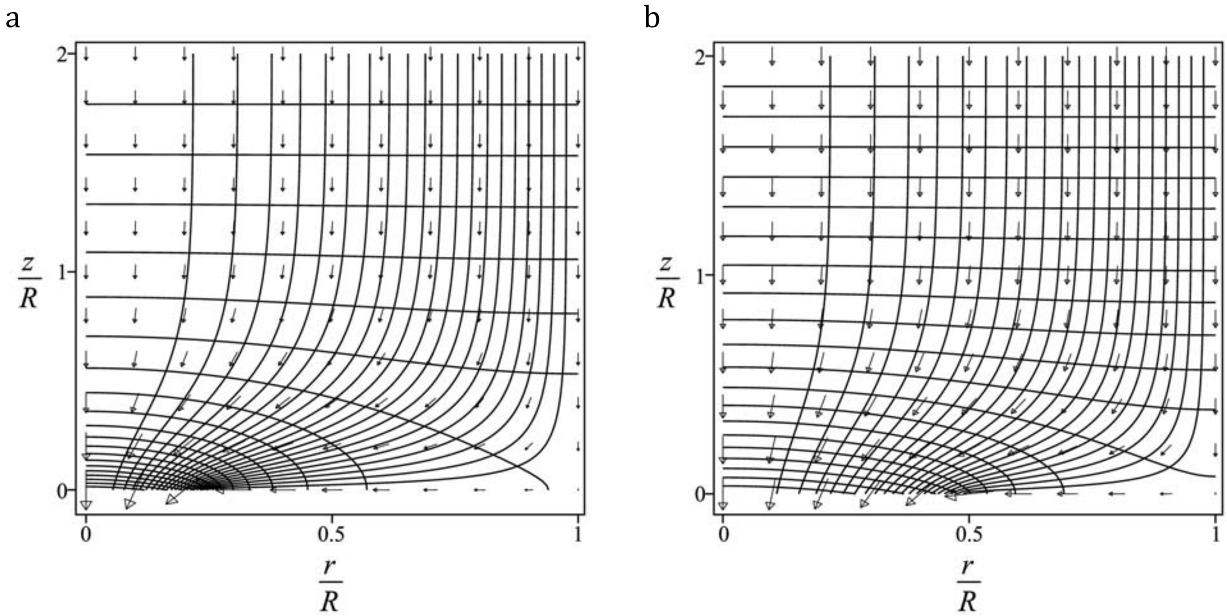

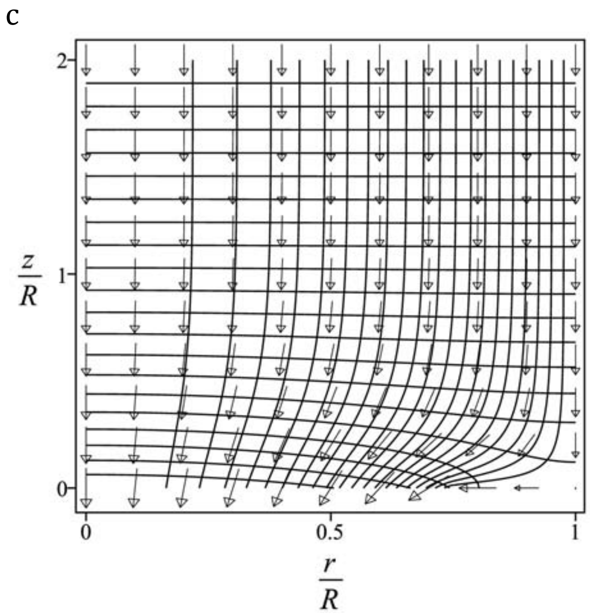

Fig. 4. Darcy flux vectors (arrows), hydraulic head contours (approximately horizontal lines) and streamlines (lines parallel to flux vectors) calculated for the solution presented in §4.2, Eqs. (27) and (28). Parameters used in all plots: $\frac{L}{R} = 2$, $\frac{Q}{K} = -1$ and $\frac{\phi_L}{R} = 20$. The plots show the effect of varying the radius of the orifice, $\frac{r_n}{R}$, at $z = 0$ (Fig. 1). Values of $\frac{r_n}{R}$ used are a: 0.25; b: 0.5; c: 0.75.

Nonetheless, the conditions given in Eqs. (22) and (23) are based on the magnitude of the disturbance relative to its initial magnitude. In the extreme case of a small orifice (r_n small), the magnitude of disturbance at some distance from the boundary in the column could be large in absolute terms, even though it is small relative to the magnitude of the disturbance at $z = 0$. This important case will be considered shortly.

An example of the exact results presented in this sub-section can be found in Fig. 4. As described in the figure caption, three cases of the orifice radius (Fig. 1) are considered. Recall that, even though r_n is varying, the total flux is the same for all cases, i.e., $Q\pi R^2$. Thus the magnitude of the flux exiting the column increases with decreasing r_n. In each case, however, visual inspection of the head contours and streamlines suggests that the dissipation length scale is of the order of the column radius, R. Nevertheless, it is also clear that the spatial variability in the applied flux disappears as $r_n \to R$. As mentioned above, this figure is based on the decay of disturbances within the column relative to the maximum variation at the $z = 0$ boundary.

In order to examine further the behavior of the orifice-induced disturbance, the relative change in maximum longitudinal flux was calculated analytically. The result is given in Eq. (50). As suggested by the plots in Fig. 4, at any fixed z the maximum longitudinal flux magnitude is at $r = 0$, with the minimum at $r = R$, independent of the flow direction. Eq. (50) was derived for the semi-infinite column solution Eq. (29) rather than the finite domain solution Eq. (27) as the boundary condition at $z = L$ in the latter enforces uniform flow at that boundary. That is, this boundary condition acts to reduce any disturbances in the flow. On the other hand, for the semi-infinite domain solution the disturbances emanating from the $z = 0$ boundary are influenced only by the flow domain, and so represents the worst case in terms of their dissipation.

Fig. 5 shows the dissipation of the maximum of the relative longitudinal flux difference as it varies with distance z from the $z = 0$ boundary, where this quantity is defined by $max_{0 \le r_n \le R}\, ln\left[50\frac{q_z(0,z)-q_z(R,z)}{q_z(0,0)-q_z(R,0)}\right]$. Again, the factor 50 included in the natural logarithm scales the result such that the horizontal axis defines a factor 50 reduction from the maximum disturbance at $z = 0$. The plot shows that the maximum length to achieve a factor 50 reduction is $\frac{z}{R} \approx 1.12$. Note also that the slope of the line is close to $\alpha_2 \approx 3.8$, showing again the dominance of the first term in the summation on the right side of Eq. (29).

Although the relative difference metric used above provides insight into the dissipation length scale, it was noted above that another applicable criterion is the absolute head difference. That is, if the maximum head difference at a given z is less than a specified value, then the flow is deemed to be uniform. This condition was investigated, again using the semi-infinite solution Eq. (27) so as to consider the maximum propagation of the boundary distur-

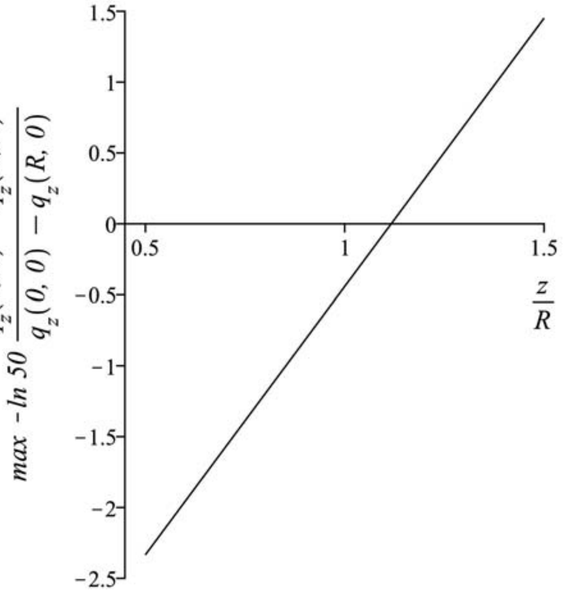

Fig. 5. Maximum relative difference in longitudinal flux as it varies with $\frac{z}{R}$, relative to that at $z = 0$, for the orifice boundary condition considered in §4.2. The flux was calculated using Eq. (29). For any z, the maximum is taken over r_n in the range $0 \leq \frac{r_n}{R} \leq 1$. The factor 50 in the relative flux causes the horizontal axis to locate where a factor 50 reduction in the maximum flux is achieved, here at $\frac{z}{R} \approx 1.12$. No matter what the size of the orifice (i.e., value is used for $\frac{r_n}{R}$), for $\frac{z}{R} \gtrsim$ 1.12 the reduction in the relative maximum flux is always in excess of 50.

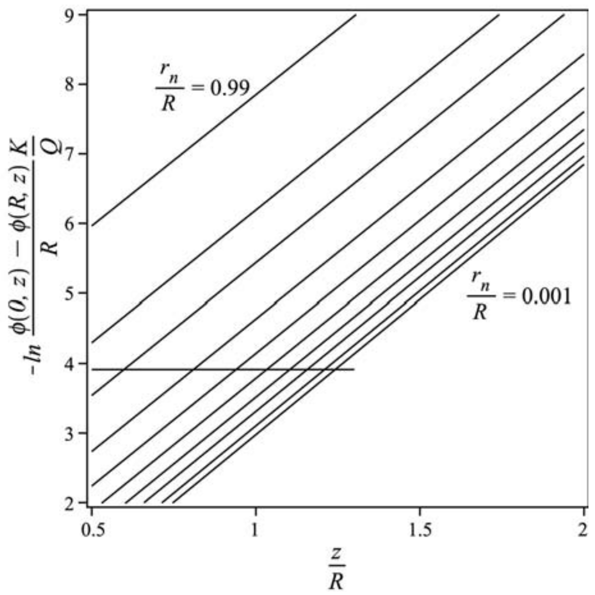

Fig. 6. Normalized maximum head difference at given z for different values of the orifice size, $\frac{r_n}{R}$, based on Eq. (29). The values for each line in the plot are, from top to bottom, $\frac{r_n}{R}$. = 0.99, 0.95, 0.9, 0.8, 0.7, 0.6, 0.5, 0.4, 0.25, 0.001. The horizontal line within the plot shows where the normalized head difference equals 0.02. Note that the various curves for each value of $\frac{r_n}{R}$ are close to linear with slopes close to $\alpha_2 \approx 3.8$

bance. Eq. (27) suggests the appropriate dimensionless form of the head difference as $-ln\left[\frac{\phi(0,z)-\phi(R,z)}{R}\frac{K}{Q}\right]$ for a centrally located orifice, recalling that at fixed z the maximum and minimum heads occur at $r = 0$ and R. Fig. 6 plots this function as it varies with $\frac{r_n}{R}$. As before, the slope of each line in the plot is close to α_2. As r_n decreases the magnitude of the disturbance at the orifice boundary increases, and so the dissipation length scale increases also. The horizontal line in Fig. 6 shows where this normalized head difference is 0.02, which could be taken as a realistic criterion for effectively uniform flow.

The smallest value of r_n used in Fig. 6 is $\frac{r_n}{R} = 0.001$. However, the maximum length scale occurs in the limit of $r_n \to 0$. In this limit, the normalized head difference of 0.02 ($-ln(0.02) \approx 3.9$) is reached at $\frac{z}{R} \approx 1.24$. For the same case of $r_n \to 0$, the normalized head difference of 0.01 ($-ln(0.01) \approx 4.6$) is reached at $\frac{z}{R} \approx 1.42$. At $\frac{z}{R} = \frac{3}{2}$, the minimum normalized head difference is about 0.0072 ($-ln(0.0072) \approx 4.9$). All these values are virtually the same as the case of $\frac{r_n}{R} = 0.001$ in Fig. 6. Thus, Fig. 6 covers the complete range of $\frac{r_n}{R}$.

It was noted above that, in Fig. 3, for $\frac{L}{R} \gtrsim 2.5$ the boundary disturbances do not interact to any significant extent (in Fig. 3 both boundaries produce disturbed flow). Consistent with this and as just mentioned in the foregoing paragraph, the horizontal line in Fig. 6 shows the maximum length scale of about $\frac{z}{R} \approx 1.24$ for a disturbance emanating from the $z = 0$ boundary. This result was checked for a finite, rather than a semi-infinite, column, by recalculating the normalized head difference with Eq. (27) rather than Eq. (29), again for the worst case of $r_n \to 0$. For the case of $\frac{L}{R} = 2.5$ there is no numerical difference with the results presented in Fig. 6 for $\frac{r_n}{R} = 0.001$. For $\frac{L}{R} = 2$ the differences with the values presented above are only in the final digit, while for $\frac{L}{R} = \frac{3}{2}$, for which the boundary disturbances are expected to interact, the normalized head differences of 0.02 and 0.01 were reached at $\frac{z}{R} \approx 1.21$ and 1.33, respectively. These calculations confirm the validity of the results in Fig. 6 to small-aspect-ratio soil columns, not just the semi-infinite case.

5. Discussion

Experiments involving Magnetic Resonance Imaging (MRI) provide detailed measurements of flow and transport within laboratory columns, at spatial scales of the order of pore diameters [14][20]. Here, two experiments reported previously in the literature are considered.

Greiner et al. [18] used MRI to trace water and solute tracer movement in saturated laboratory columns filled with glass beads. Data were collected with a spatial resolution of 2.34 mm. One column used uniform glass beads of radius of about 0.5 mm, the other column comprised a heterogeneous medium. The column dimensions were 282 mm length with a radius of 95 mm. At the column entrance water and solute were injected pseudo-uniformly through an array of 19 injection tubes, each having a radius of 2 mm. The column exit, however, drained through a single orifice. Thus, the experimental setup is consistent with the layout and boundary conditions used in §4.2, except that their drain location was at the top of the experimental apparatus, rather than at the bottom as displayed in Fig. 1. Greiner et al. [18] reported that a "nonuniform velocity profile is seen in each of the columns (Plates 1-4). The nonuniform profile is emphasized in the upper third of the column, where the single discharge exit does not permit a cross-sectionally homogeneous flow distribution (Plates 1 and 3, steps 11-15; Plates 2 and 4, steps 7-13)." Plate 3 (Step 13) [18] shows a tracer moving into the exit orifice, which had a radius of about 10 mm (estimated by eye). The flow convergence towards the orifice extended to about 100 mm longitudinally. That is, the disturbance to the flow was of order of the column radius, in agreement with the above analysis. Although this estimate is imprecise, it is clear that the length scale evident in the experimental results is consistent with the theoretical estimate.

Deurer et al. [16] carried out a thorough analysis of flow in a column of length 46 mm and radius 7 mm, filled with glass beads of radius 1 mm. Tubes supplying and draining the column had a radius of 0.865 mm, leading to disturbed flow patterns in the regions near each end of the experimental column. The spatial resolution of the data presented was 156 μm. The analysis in [16] evaluated the impact of the measurement scale by considering data based on increasing sample volumes of the porous medium, with all samples centered on the column mid-point. Thus, with increasing volume size, the impact of the disturbed flow regions at each end of the column became evident, although the flow patterns in these zones were not reported. Based on these spatially integrated observations of the spatially distributed local flow velocities, Deurer et al. [16] concluded that the disturbed flow patterns influenced about half the column, i.e., to a distance of about 11.5 mm from each of the entrance and exit surfaces, which is about 50% larger than the estimate of 7 mm based on the column radius alone. Deurer et al. [16] based their estimate on their Fig. 1A, which shows the average velocity as it varies with sample volume. However, it is clear from this figure, as well as the velocity variances presented in their Fig. 2, that their estimate of the disturbed zone length of 11.5 mm is not a precise value, and that a smaller disturbed zone length could also be consistent with the data presented.

An additional consideration is the size of the glass beads (radius 1 mm) relative to the column radius (7 mm) and the radius of the supply and drainage tubes (0.865 mm). Deurer et al. [16] estimated the length scale at which flow can be considered as a continuum to be around 4 – 5 mm. Since this is the order of the column radius, it is possible that the flow at the entrance and exit regions did not behave as continua governed by Laplace's equation, which is a fundamental assumption in the analysis presented here. Referring to solute transport, Deurer et al. [16] distinguished the transition between stochastic-convective transport and convective-dispersive transport at the length scale of a few mm. Since the continuum assumption is fundamental to application of the governing model, one viewpoint could be to take the plane at 4 or 5 mm from the boundary to be the location of the continuum boundary condition. Then, adding the column radius of 7 mm gives a total disturbed zone very close to the estimate of Deurer et al. [16]. Irrespective of this, the theoretical estimate of about one column radius as the dissipation length scale and the experimental analyses of Deurer et al. [16] are consistent in that they are of similar magnitude.

Solute dispersivity is a key parameter derived from soil column experiments. The question of the factors affecting dispersion estimates from such experiments, as well as that of "apparatus-induced" dispersion, was examined by Bromly et al. [12]. They carried out an exhaustive statistical examination of 216 published experiments focusing on the reported dispersivities and their relation to a range of experimental factors, including flow velocity, clay and silt content, bulk density, and column diameter and length. They reported increased dispersivity with column diameter, opining that the "increased dispersivities could be an expression of a lateral scale effect." This view and the statistical evidence presented in [12] are consistent with the influence of the column radius found here.

6. Conclusion

A general exact solution for axisymmetric steady flow in a soil column filled with homogeneous soil has been used to analyze theoretically the effect of nonuniform boundary conditions on flow within the column. The analysis enables an estimation of the longitudinal dissipation length scale arising from radially symmetric disturbances introduced at the column entrance or exit. In all cases, and regardless of the flow direction, the analysis reveals that this length is, for practical purposes, of the order of the column radius. In the most extreme case examined, that of a very narrow tube supplying/removing water through an orifice at one end of the column, at a distance of $\frac{3}{2}$ column radii from the orifice the normalized absolute head difference reduced to 0.0072. It is suggested that this distance, $\frac{3}{2}$ column radii, represents the extreme upper bound of the region of boundary condition-induced disturbed flow in a column. This means that, independent of the boundary conditions, a column with a length to radius ratio in excess of 3 will have a region on uniform flow within it. These results can be adapted to the case of a homogeneous anisotropic soil via a simple scaling.

An immediate practical consequence is that flow in soil columns will be uniform if at each end of the column a baffle region, with a length of about the column radius, is incorporated. The theory shows it is irrelevant what material is in the baffle zone, so long as (i) the flow there satisfies Laplace's equation and (ii) the boundary between the two zones is perpendicular to the longitudinal axis. Because of (i), as the flow passes through the baffle region, nonuniformities in the flow are attenuated such that the head profile perpendicular to the longitudinal axis becomes effectively uniform, at least compared with the profile at the column boundary (location of the maximum disturbance magnitude). As a result of (ii), the streamlines exiting the baffle zone are not refracted since they are essentially perpendicular to the boundary between the two zones. Furthermore, if the baffle zone is separated from the soil by a perforated plate, then as the flow passes through the plate, any residual radial components of the flow will be physically further attenuated by the perforations. Finally, while the use of a baffle zone will provide a uniform flow within the soil column, if the column is used to investigate solute transport phenomena, the nonuniform flow introduces "apparatus-induced" dispersion, which should be accounted for in the solute data analysis.

Appendix 1. General solution to the Laplace equation model for axisymmetric flow in a cylinder containing a homogeneous soil

Here the solution satisfying Eqs. (1) – (5) is derived based on separation-of-variables following, e.g., [11]. To this end, let:

$$\phi(r,z) = \mathcal{R}(r)Z(z), \tag{31}$$

then Eq. (1) becomes:

$$\frac{1}{\mathcal{R}r}\frac{\mathrm{d}}{\mathrm{d}r}\left(r\frac{\mathrm{d}\mathcal{R}}{\mathrm{d}r}\right) + \frac{1}{Z}\frac{\mathrm{d}^2Z}{\mathrm{d}z^2} = 0. \tag{32}$$

Let:

$$\frac{\mathrm{d}^2Z}{\mathrm{d}z^2} = \frac{\alpha^2}{R^2}Z, \tag{33}$$

in which case Eq. (32) is:

$$\frac{\mathrm{d}}{\mathrm{d}r}\left(r\frac{\mathrm{d}\mathcal{R}}{\mathrm{d}r}\right) + \mathcal{R}r\frac{\alpha^2}{R^2} = 0. \tag{34}$$

The general solution to Eq. (33) is:

$$Z(z) = C_1\exp\left(\alpha\frac{z}{R}\right) + C_2\exp\left(-\alpha\frac{z}{R}\right) \tag{35}$$

and that for Eq. (34) is:

$$\mathcal{R}(r) = C_3\mathrm{J}_0\left(\alpha\frac{r}{R}\right), \tag{36}$$

where J_v is the v^{th}-order Bessel function of the first kind. Eq. (36) ensures the solution satisfies Eq. (2) for arbitrary $\frac{\alpha}{R}$. However, to satisfy Eq. (3) values of α are limited to solutions of:

$$\mathrm{J}_1(\alpha) = 0. \tag{37}$$

Denote the nonnegative values of α satisfying Eq. (37) as α_1, α_2, etc. The first four values are: $\alpha_1 = 0, \alpha_2 \approx 3.8317, \alpha_3 \approx 7.0156, \alpha_4 \approx 10.173$. The asymptotic form of α_i is $\left(i - \frac{3}{4}\right)\pi$ (e.g., [9]). The first nonnegative value, $\alpha_1 = 0$, cannot be used in any meaningful way in the solution [11] as it is identically zero for any r in Eq. (36).

A solution is proposed of the form:

$$\phi(r,z) = A_1 + B_1 z + \sum_{i=2}^{\infty}\left[A_i \exp\left(\alpha_i \frac{z}{R}\right) + B_i \exp\left(-\alpha_i \frac{z}{R}\right)\right] \mathrm{J}_0\left(\alpha_i \frac{r}{R}\right), \tag{38}$$

where the values of α are defined by Eq. (37). Eq. (38) satisfies Eqs. (1) – (3), with the coefficients A and B chosen to satisfy Eqs. (4) and (5). The main step in determining the coefficients is expanding the boundary condition functions $g(r)$ and $\phi_L(r)$ in Eqs. (4) and (5), respectively, as Fourier-Bessel series following Eqs. (39) and (40). To distinguish each expansion, the coefficients – i.e., $\mathcal{F}_i$ in Eqs. (39) and (40) – corresponding to the expansion of $g(r)$ are denoted as D_i while those for $\phi_L(r)$ are denoted as E_i.

Appendix 2. Background on Fourier-Bessel series and Bessel functions

The function, $f(r), 0 \le r \le R$, can be expanded in a Fourier-Bessel series [11] as:

$$f(r) = \frac{2}{R^2}\int_0^R r\, f(r)\mathrm{d}r + \sum_{i=2}^{\infty} \mathcal{F}_i \mathrm{J}_0\left(\alpha_i \frac{r}{R}\right), 0 \le r \le R, \tag{39}$$

where the coefficients, $\mathcal{F}_i$, are given by:

$$\mathcal{F}_i = \frac{2}{R^2}\frac{\int_0^R r\, f(r)\mathrm{J}_0\left(\alpha_i \frac{r}{R}\right)\mathrm{d}r}{\mathrm{J}_0^2(\alpha_i)}, i = 2, 3, \cdots. \tag{40}$$

Other results used are (e.g., [1]):

$$\frac{\mathrm{dJ}_0\left(\alpha_i \frac{r}{R}\right)}{\mathrm{d}r} = -\frac{\alpha_i}{R}\mathrm{J}_1\left(\alpha_i \frac{r}{R}\right), \tag{41}$$

$$r\frac{\mathrm{dJ}_1\left(\alpha_i \frac{r}{R}\right)}{\mathrm{d}r} = \alpha_i \frac{r}{R}\mathrm{J}_0\left(\alpha_i \frac{r}{R}\right) - \mathrm{J}_1\left(\alpha_i \frac{r}{R}\right) \text{ and} \tag{42}$$

$$\frac{\mathrm{d}\left[r\mathrm{J}_1\left(\alpha_i \frac{r}{R}\right)\right]}{\mathrm{d}r} = \alpha_i \frac{r}{R}\mathrm{J}_0\left(\alpha_i \frac{r}{R}\right). \tag{43}$$

Appendix 3. Dissipation length metrics

As described in §4.1, the quantity $\frac{\phi(0,z)-\phi(R,z)}{\phi(0,L)-\phi(R,L)}$ is used to determine the length scale over which variations in the boundary condition at $z = L$ dissipate. Eq. (17) is written, with $q_z(0,0) = q_z(R,0)$, as:

$$\phi(0,z) = \phi(R,L) + \frac{\phi(0,L)-\phi(R,L)}{1-\mathrm{J}_0(\alpha_i)}\left[\frac{\cosh\left(\alpha_i \frac{z}{R}\right)}{\cosh\left(\alpha_i \frac{L}{R}\right)} - \mathrm{J}_0(\alpha_i)\right] + (L-z)\frac{q_z(R,0)}{K}. \tag{44}$$

Similarly,

$$\phi(R,z) = \phi(R,L) + \frac{\phi(0,L)-\phi(R,L)}{1-\mathrm{J}_0(\alpha_i)}\left[\frac{\cosh\left(\alpha_i \frac{z}{R}\right)}{\cosh\left(\alpha_i \frac{L}{R}\right)} - 1\right]\mathrm{J}_0(\alpha_i) + (L-z)\frac{q_z(R,0)}{K}. \tag{45}$$

Using Eqs. (44) and (45) gives, for $\frac{\phi(0,z)-\phi(R,z)}{\phi(0,L)-\phi(R,L)}$:

$$\frac{\phi(0,z)-\phi(R,z)}{\phi(0,L)-\phi(R,L)} = \frac{\cosh\left(\alpha_i \frac{z}{R}\right)}{\cosh\left(\alpha_i \frac{L}{R}\right)}. \tag{46}$$

Eq. (46) is exact and can be used directly to calculate the dissipation length scale. If the arguments on the right side of Eq. (46) are sufficiently large, then they can be approximated by exponentials, giving the simple result in Eq. (19). On the other hand, Eq. (46) can be solved directly for z. If the left side of Eq. (46) is set equal to M^{-1} then

$$z = \frac{R}{\alpha_i}\operatorname{arccosh}\left[M^{-1}\cosh\left(\alpha_i \frac{L}{R}\right)\right]. \tag{47}$$

The relative error of the approximation Eq. (19) can easily be calculated using the exact result in Eq. (47). The relative error, E, is defined as:

$$\mathrm{E} = \left|1 - \frac{\alpha_i \frac{L}{R} - \ln(M)}{\operatorname{arccosh}\left[M^{-1}\cosh\left(\alpha_i \frac{L}{R}\right)\right]}\right|. \tag{48}$$

For the case considered in §4.1, i.e., $i = 2$ and M=50, Eq. (48) gives $E < 1\%$ for $\frac{L}{R} \gtrsim 1.5$. As $\frac{L}{R}$ increases, the relative error decreases rapidly. For example, for $\frac{L}{R} = 2$, E ≈ 0.015%. That is, Eq. (19) is sufficiently accurate to estimate the dissipation length scale.

The other case considered in §4.1 is a nonuniform flux applied at $z = 0$ and a uniform head condition at $z = L$. From Eq. (17), with $\phi(0, L) = \phi(R, L)$, the disturbance dissipation is given by:

$$\frac{\phi(0,z) - \phi(R,z)}{\phi(0,0) - \phi(R,0)} = \frac{\sinh\left(\alpha_i \frac{L-z}{R}\right)}{\sinh\left(\alpha_i \frac{L}{R}\right)} \approx \exp\left(-\alpha_i \frac{z}{R}\right), \tag{49}$$

where the approximation is that mentioned in §4.1, Eq. (22). Using a calculation similar to that presented just above, the relative error of this approximation is less than 1% for $\frac{L}{R} \gtrsim 1.4$.

The next case considered is that of the orifice, described in §4.2. One metric to estimate the dissipation length scale is the maximum range of the longitudinal flux at any cross-section, scaled relative to that at $z = 0$, i.e., $\frac{q_z(0,z) - q_z(R,z)}{q_z(0,0) - q_z(R,0)}$. For clarity, the solution for the semi-infinite column, Eq. (29), is used to calculate the flux, i.e., the analysis is applicable for columns with small aspect ratios, yielding:

$$\frac{q_z(0,z) - q_z(R,z)}{q_z(0,0) - q_z(R,0)} = \frac{2r_n}{R} \sum_{i=2}^{\infty} \frac{J_1\left(\alpha_i \frac{r_n}{R}\right)}{\alpha_i J_0^2(\alpha_i)} \exp\left(-\alpha_i \frac{z}{R}\right) [1 - J_0(\alpha_i)]. \tag{50}$$

References

[1] Abramowitz M, Stegun IA, eds. Handbook of mathematical functions with formulas, graphs, and mathematical tables. Washington DC, USA: National Bureau of Standards Applied Mathematics Series No. 55, 1964.

[2] Bajracharya K, Barry DA. Nonequilibrium solute transport parameters and their physical significance: Numerical and experimental results. J Contam Hydrol 1997;24(3-4),185-204.

[3] Bajracharya K, Tran YT, Barry DA. Cadmium adsorption at different pore water velocities. Geoderma 1996;73(3-4),197-216.

[4] Barry DA, Sposito G. Application of the convection-dispersion model to solute transport in finite soil columns. Soil Sci Soc Am J 1988;52(1),3-9.

[5] Batchelor G. An introduction to fluid dynamics. Cambridge, UK: Cambridge University Press, 1967.

[6] Bear J. Dynamics of fluids in porous media. New York, New York, USA: American Elsevier, 1972.

[7] Bear J. Some experiments in dispersion. J Geophys Res 1961;66(8),2455-67.

[8] Benker E, Davis GB, Barry DA. Estimating the retardation coefficient of trichloroethene for a sand aquifer low in sediment organic carbon - A comparison of methods. J Contam Hydrol 1998;30(1-2),157-78.

[9] Beyer WH. Handbook of the mathematical sciences, 5th ed. West Palm Beach, Florida, USA: CRC Press, 1978.

[10] Biggar JW, Nielsen DR. Diffusion effects in miscible displacement occurring in saturated and unsaturated porous materials. J Geophys Res 1960;65(9),2887-95.

[11] Bland DR. Solutions of Laplace's equation. Glencoe, Illinois, USA: The Free Press; 1961.

[12] Bromly M, Hinz C, Aylmore LAG. Relation of dispersivity to properties of homogeneous saturated repacked soil columns. Eur J Soil Sci 2007;58(1),293-301.

[13] Brusseau ML. The influence of solute size, pore water velocity, and intraparticle porosity on solute dispersion and transport in soil. Water Resour Res 1993;29(4),1071-80.

[14] Chen Q, Kinzelbach W, Oswald S. Nuclear magnetic resonance imaging for studies of flow and transport in porous media. J Environ Qual 2002;31(2),477–86.

[15] Culligan PJ, Barry DA, Parlange J-Y, Steenhuis TS, Haverkamp R. Infiltration with controlled air escape. Water Resour Res 2000;36(3),781-5.

[16] Deurer M, Vogeler I, Clothier BE, Scotter DR. Magnetic resonance imaging of hydrodynamic dispersion in a saturated porous medium. Transp Porous Media 2004;54(2),145-66.

[17] Dutt GR, Tanji KK. Predicting concentrations of solutes in water percolated through a column of soil. J Geophys Res 1962;67(9),3437-9.

[18] Greiner A, Schreiber W, Brix G, Kinzelbach W. Magnetic resonance imaging of paramagnetic tracers in porous media: Quantification of flow and transport parameters. Water Resour Res 1997;33(6),1461-73.

[19] Happel J, Brenner H. Low Reynolds number hydrodynamics, with special applications to particulate media. The Hague, The Netherlands: Martinus Nijhoff; 1983.

[20] Herrmann K-H, Pohlmeier A, Gembris D. Vereecken H. Three-dimensional imaging of pore water diffusion and motion in porous media by nuclear magnetic resonance imaging. J Hydrol 2002;267(3-4),244-57.

[21] Hofstee C, Walker RC, Dane JH. Infiltration and redistribution of perchloroethylene in stratified water-saturated porous media. Soil Sci Soc Am J 1998;62(1),13-22.

[22] James RV, Rubin J. Accounting for apparatus-induced dispersion in analysis of miscible displacement experiments. Water Resour Res 1972;8(3),717-21.

[23] Jeong J-T, Choi S-R. Axisymmetric Stokes flow through a circular orifice in a tube. Phys Fluids 2005;17(5),1-5.

[24] Li L, Barry DA, Culligan-Hensley PJ, Bajracharya K. 1994. Mass transfer in soils with local stratification of hydraulic conductivity. Water Resour Res 1994;30(11),2891-900.

[25] Li L, Barry DA, Stone KJL. Centrifugal modelling of nonsorbing, nonequilibrium solute transport in a locally inhomogeneous soil. Canadian Geotech J 1994;31(4),471-7.

[26] Massabò M, Catania F, Paladino O. A new method for laboratory estimation of the transverse dispersion coefficient. Ground Water 2007;45(3),339-47.

[27] Miretzky P, Munoz C, Carrillo-Chavez A. Experimental Zn(II) retention in a sandy loam soil by very small columns. Chemosphere 2006;65(11),2082-9.

[28] Nielsen JM, Pinder GF, Kulp TJ, Angel SM. Investigation of dispersion in porous media using fiber-optic technology. Water Resour Res 1991;27(10),2743–9.

[29] Roychoudhury AN. Dispersion in unconsolidated aquatic sediments. Estuar Coast Shelf Sci 2001;53(5),745-57.

[30] Spanier J, Oldham KB. An atlas of functions. New York, New York, USA: Hemisphere, 1987.

[31] Spiegel MR, Mathematical handbook of formulas and tables, 2nd edition. New York, New York, USA: McGraw-Hill, 2006.

[32] Starr JL, Parlange J-Y. Plate-induced tailing in miscible displacement experiments. Soil Sci 1977;124(1),56-60.

[33] Steffy DA, Johnston CD, Barry DA. Numerical simulations and long-column tests of LNAPL displacement and trapping by a fluctuating water table. J Soil Contam 1998;7(3),325-56.

[34] Tran YT, Bajracharya K, Barry DA. Anomalous cadmium ad-sorption in flow interruption experiments. Geoderma 1998;84(1-3),169-84.

[35] Tsang DCW, Lo IMC. Influence of pore-water velocity on transport behavior of cadmium: Equilibrium versus nonequilibrium. Pract Period Hazard, Toxic Rad Waste Manage 2006;10(3),162-70.

[36] Wang H, Persaud N. Miscible displacement of initial solute distributions in laboratory columns. Soil Sci Soc Am J 2004;68(5),1471-8.

[37] Watson SJ, Barry DA. Numerical analysis of stable brine displacements for evaluation of density-dependent flow theory. Phys Chem Earth, Part B. Hydrol, Oceans Atmos. 2001;26(4),325-31.

[38] Watson SJ, Barry DA, Schotting RJ, Hassanizadeh SM. On the validity of Darcy's Law for stable high-concentration displacements in granular porous media. Transp Porous Media 2002;47(2),149-67.

[39] Zill DG, Cullen MR. Advanced engineering mathematics. Boston, USA:PWS-Kent, 1992.